

A high-speed hyperspectral imaging system and large-scale hyperspectral dataset for abdominal surgical applications

Kelden Pruitt^{a,b}, Weston DeAtley^{a,b}, Armand Rathgeb^{a,b},
Brett Johnson^c, Jeffrey Gahan^c, Baowei Fei^{a,b,d*}

^a University of Texas at Dallas, Center for Imaging and Surgical Innovation, Richardson, TX

^b University of Texas at Dallas, Department of Bioengineering, Richardson, TX

^c University of Texas Southwestern Medical Center, Department of Urology, Dallas, TX

^d University of Texas Southwestern Medical Center, Department of Radiology, Dallas, TX

* Corresponding author: bfei@utdallas.edu, Website: <https://fei-lab.org>

ABSTRACT

Modern foundation models have shown promise in classification tasks and may be used in medical imaging systems, but the current imaging modalities, such as fluorescence and narrow-band imaging, have drawbacks hindering the ability to generate the large datasets required of current computer vision (CV) models. Hyperspectral imaging (HSI) is a non-invasive and label-free modality and has shown promise in tissue classification and cancer detection. But, to leverage the rich information provided with HSI alongside modern CV architectures, larger datasets must be curated. As such, we have designed an HSI system and workflow to address this gap by allowing for high-throughput *ex vivo* tissue imaging. We utilize an optical configuration consisting of three hyperspectral cameras along with a custom in-house application for efficient imaging. The system covers a wavelength range of 460-960 nm, acquiring 30 hyperspectral images that are averaged into a single hypercube with 55 bands, a process completed in under 6 seconds. The system has been used to acquire 1835 hyperspectral images of tissues from four animal models including porcine, murine, galline, and bovine organs. The high-speed HSI system and the corresponding dataset can be further applied to many minimally invasive surgical applications including robotic-assisted laparoscopic surgery.

Keywords: Hyperspectral imaging, minimally invasive surgery, dataset creation, foundation model, laparoscopy

1. INTRODUCTION

Minimally invasive surgery (MIS) has benefitted greatly from technological advances and improvements leading to high-quality visualization of the surgical field, including 4k RGB and stereoscopic systems. Other advances, such as fluorescence and narrow-band imaging have pushed the field further with the goal of assisting surgeons to identify key structures intraoperatively. Hyperspectral imaging (HSI) presents a promising alternative and improvement to RGB modalities, offering a richer dataset that captures spectral and spatial information across a broad spectrum of light [1]. Previous works have shown that HSI can outperform traditional RGB imaging in classification tasks when using CNN architectures [2-4]. This suggests a significant potential for HSI to enhance the feature-extraction capabilities of large foundation models further by providing more information than the RGB images commonly used. To realize this potential, there is a critical need for the development of extensive HSI datasets, akin to those used in established computer vision (CV) works. The goal of our work is to address this need by developing a high-throughput, rapid HSI system for *ex vivo* tissues. The system aims to facilitate the acquisition of large-scale datasets, thereby paving the way for the integration of data-rich HSI with cutting-edge transformer architectures. Such an integration could lead to the development of powerful tools for minimally invasive surgery, enhancing both diagnostic and therapeutic outcomes.

Foundation models have seen remarkable advancements in recent years, largely driven by the availability of large public datasets combined with sophisticated architectures. Notable models such as DINOv1 [5], DINOv2 [6], and masked autoencoders [7] have leveraged these datasets to achieve impressive performance across various tasks. These datasets include ImageNet-1K [8], COCO [9], and ADE20K [10], which vary in size from tens of thousands of images (ADE20K) to millions of images (ImageNet). Different datasets are utilized for different downstream tasks, as segmentation sets require corresponding masks instead of single, image-wide captions for classification models. However, while these datasets have been widely used in general CV models, they are limited in their ability to contribute to the domain of

medical imaging. There is a need for the curation of large-scale datasets for medical imaging tasks, such as Mass-100K, The Cancer Genome Atlas, and Providence, all of which contain thousands of H&E stained histopathology slides that have been used in the training and evaluation of whole-slide digital pathology models including UNI [11], CONCH [12], and Prov-GigaPath [13]. But, these works utilize RGB data and are confined to pathologic applications.

Within HSI, numerous datasets exist for the training of classification and spectral unmixing deep learning models. That said, most of these datasets are specific to remote sensing applications and are limited in their overall size, with some of the most commonly used datasets consisting of a single hypercube, as shown in Table 1. Large-scale datasets are often required in order to train larger CV models. Within medical HSI specifically, few datasets exist for this purpose. The aim of this work is to address this discrepancy by curating a large database of hyperspectral images of abdominal and reproductive tissues for medical applications.

Table 1. Existing HSI datasets for deep learning model training and evaluation.

Dataset	# Images	Raster Size	Wavelength Range	# Bands	# Classes	Application
Indian Pines [14]	1	145 x 145	200 – 2500	224, 200*	16	RS – Segmentation
PaviaU [15]	1	610 x 340	430 – 860	115, 103*	9	RS – Segmentation
Houston2018 [16]	1	1202 x 4172	380 – 1050	144, 48*	20	RS – Segmentation
Salinas	1	512 x 217	360 – 2500	224, 204*	16	RS – Segmentation
Botswana [17]	1	1476 x 256	400 – 2500	242, 145*	14	RS – Segmentation
Kennedy Space Center [17]	1	512 x 614	400 – 2500	224, 176*	13	RS – Segmentation
HySpecNet-11k [18]	~11k	128 x 128	420 – 2450	224, 202*	N/A	RS – Image Compression
SpectralEarth [19]	~538k	128 x 128	420 – 2450	224, 202*	15-20**	RS – Classification, Segmentation
BigEarthNet [20]	~590k	120 x 120, 60 x 60, 20 x 20	443 - 2190	13	44	RS - Classification
In-vivo HS Brain [21]	61	741 x 1004	400 – 1000	826, 645*	4	Medical image Classification
HyperGlobal-450k [22]	~447k	64 x 64	400 – 2500	242, 175*, 330, 150*	N/A	RS – Pre-training
HeiPorSPECTRAL [23]	~5700	480 x 640	500 – 1000	100	20	Medical – Classification, Segmentation

*After data cleaning and band removal. **Classes on subsets of the network for different applications. RS – Remote Sensing.

2. METHODS

When approaching the design of our system, two primary objectives were considered. First, the system needed to cover a wide spectral range to not limit the scope and potential application of the dataset. Second, the system needed to allow for high-throughput imaging via fast image acquisition times.

2.1 Imaging Setup

The proposed imaging system includes an optical configuration that allows three snapshot hyperspectral cameras to be used simultaneously. The hardware of the system is shown in Figure 1. The setup consists of a 10 mm, 0° laparoscope (Olympus UHD) and a 150-Watt halogen light source (OSLIR High-Intensity Fiber-Coupled Illuminator, Thorlabs, Newton, NJ) with an output power density covering 400 – 1750 nm. A fabricated adapter couples the laparoscope to a 605 nm dichroic mirror (Thorlabs, Newton, NJ) where incoming light reflects into the visible (VIS) hyperspectral camera, which covers a wavelength range of 460 – 600 nm. Transmitted light enters a 50:50 beam splitter (Non-Polarizing NIR Cube Beamsplitter, Edmund Optics) to which the red/near-infrared (RNIR) and near-infrared (NIR) hyperspectral cameras are attached, covering wavelength ranges of 600 – 870 nm and 660 – 960 nm, respectively. A 35-mm VIS-NIR C-mount lenses are used with each hyperspectral camera along with 1.5× lens extenders to utilize the imaging sensor to a greater degree.

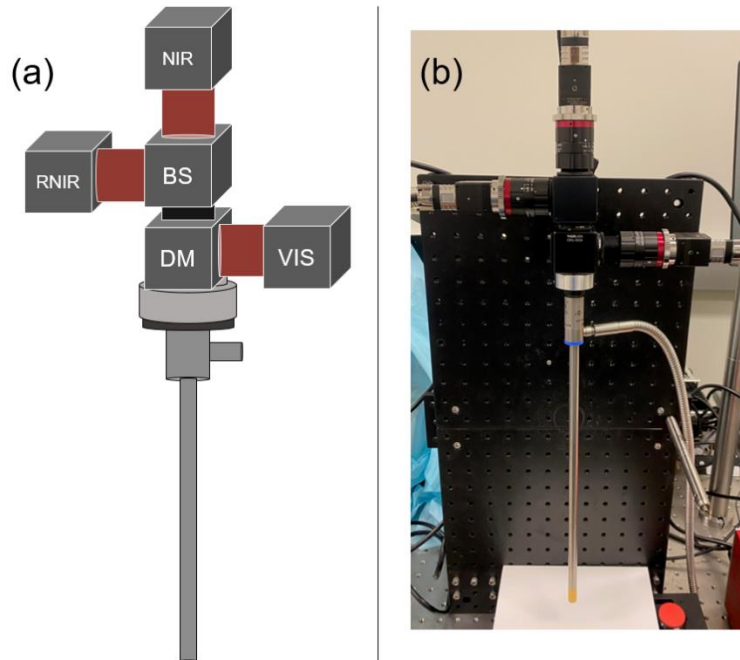


Figure 1. Hardware setup of the high-speed hyperspectral laparoscopic imaging system. A) Schematic of system. B) Constructed system with validation reflectance tile. (DM: Dichroic mirror. BS: Beam splitter. VIS: Visible hyperspectral camera. RNIR: Red/near-infrared hyperspectral camera. NIR: Near-infrared hyperspectral camera.)

2.2 Image Acquisition

To enable high-speed imaging, a custom software was developed in C++ using an application programming interface (API) along with the QT graphical user interface framework as covered in our previous work [24]. First, the optical configuration of each camera utilized is set, including $f/\#$, focal length, and exit pupil distance. Then, dark current references are acquired for each camera with the light source and room lights off, and the distal tip of the scope covered with an optical absorbing material. Hyperspectral images from each camera are then acquired using a burst capture feature, with each camera capturing a specified number of images in sequence (10 for tissues, 20 for white reference), with more captured images leading to longer acquisition times but superior noise reduction after temporal averaging. A white reference image is acquired using a 95% reflectance tile for calibration as described in Section 2.4.

2.3 System Validation

Prior to acquiring data from *ex vivo* tissues, the spectral accuracy of the novel hardware configuration was evaluated. Utilizing a similar workflow as our previous work [25], standard reflectance tiles were used to assess the spectral accuracy of the system. Eight colored tiles with reflectance values provided from 360-830 nm along with a calibrated tile with reflectance values provided from 235-2000 nm (WCS-MC-020, Labsphere). The colored tiles present different spectral footprints and intensities and overlap the majority of bands from the system. The remaining NIR wavelengths captured by the system are covered by the NIR tile. The root-mean-squared-error (RMSE) was calculated for each tile.

2.4 Data Processing

Data processing was performed in MATLAB (MathWorks Inc, Natick, MA, USA) and included image calibration, pseudo-*RGB* construction, image registration, and spectral analysis. Hyperspectral images were calibrated according to Equation (1), where the standard used is a 95% reflectance white reference surface:

$$I_{\text{reflectance}}(\lambda) = \frac{I_{\text{processed}}(\lambda)}{I_{\text{WR}}(\lambda)} \quad (1)$$

where $I_{\text{reflectance}}$ is the calibrated reflectance intensity, $I_{\text{processed}}$ and I_{WR} are the dark current corrected reflectance intensities of the tissue/tile and the white reference, respectively. Calibrated reflectance values were used to construct a pseudo-RGB pixel by selecting bands from the VIS hyperspectral camera corresponding to red, green, and blue channels. Auto-brightness correction was applied for visualization of tissues with varying absorbance behaviors. Conversion from the red-green-blue image format to hue-saturation-value was conducted to calculate an appropriate gain for each image. Pixels only in the center of the field of view (FOV) and non-background were considered to avoid over-exposure. Respective gains were then applied to the pseudo-RGB.

Image registration was performed semi-automatically using rigid and affine transformations and applied to the RNIR and NIR hypercubes, with the VIS hypercube acting as the fixed object. Each transformation is an intensity-based approach, with Mattes mutual information algorithm used as the metric to gauge similarity [26] and an evolutionary algorithm used to update transforms iteratively [27]. Dice similarity coefficients were used to evaluate the image registration quality. The registered hyperspectral images were then concatenated to form a final hypercube of size 510 x 270 x 55. Spectral analysis was performed by manually selecting a region of interest and extracting the corresponding average spectra from the region.

2.5 Ex Vivo Tissue Imaging

Larger animal model tissues were sourced from various channels including local farms and marketplaces. Murine organs were harvested from internal lab facilities. Fluids innate to the organ environment are preserved to maintain tissue moisture levels throughout imaging, with phosphate buffer saline (PBS) solution supplemented when needed.

A dataset was created to represent a variety of organs and tissue types across multiple animal models with an emphasis on abdominal and reproductive organs often seen in MIS. Murine, porcine, bovine, and galline organs that were accessible and in the proposed domain were included in the dataset. Nine tissues were identified, representing a variety of spectral and morphological features. The working distance was varied using an adjustable stage from 7 cm for larger tissues such as bovine liver down to 3 cm for smaller tissues such as murine organs. Tissues were imaged to maximize total surface area with minimal overlap to avoid redundancy in the dataset. The number of acquired images per tissue varies with tissue type due to FOV, with up to 18 hypercubes being captured for a single porcine stomach to 2 hypercubes for murine kidney.

3. RESULTS

3.1 Validation Result

The acquired spectral curves from the reference tiles are shown in Figure 2. The triple-camera hyperspectral system with our optical configuration captures 55 spectral images from 458-939 nm. Bands beyond the coverage of the colored tiles were excluded from quantitative analysis. The system shows acceptable conformance to the various spectral footprints presented by the different tiles, which is also confirmed in the RMSE values shown in Table 2. The average RMSE across all tiles is $4.196 \pm 1.331\%$.

3.2 Ex Vivo Tissue Spectra

Imaging studies were conducted using the triple-camera setup on the proposed animal models. Resulting pseudo-RGB images along with spectral curves from different regions of a subset of tissues can be seen in Figure 3. Regions of interest were manually selected for different regions of each tissue for spectral observation. Glare pixels were left in attempt to mimic intraoperative imaging conditions, where glare is present as well. PBS was used sparingly to maintain tissue moisture levels throughout the duration of imaging. The value of capturing a wide spectral range is shown in the ability to distinguish tissue types in different wavelength ranges – such as the visibly brighter tissues (intestine and stomach) distinguishing themselves primarily in the VIS camera range as opposed to the darker/red tissues (liver, kidney, spleen) showing separation towards the RNIR/NIR region. Dice scores from the registration pipeline used for the RNIR and NIR hyperspectral images are 0.964 ± 0.014 and 0.965 ± 0.014 , respectively. To date, 1835 hypercubes of various tissues have been acquired. The breakdown by animal and organ model is shown in Table 3.

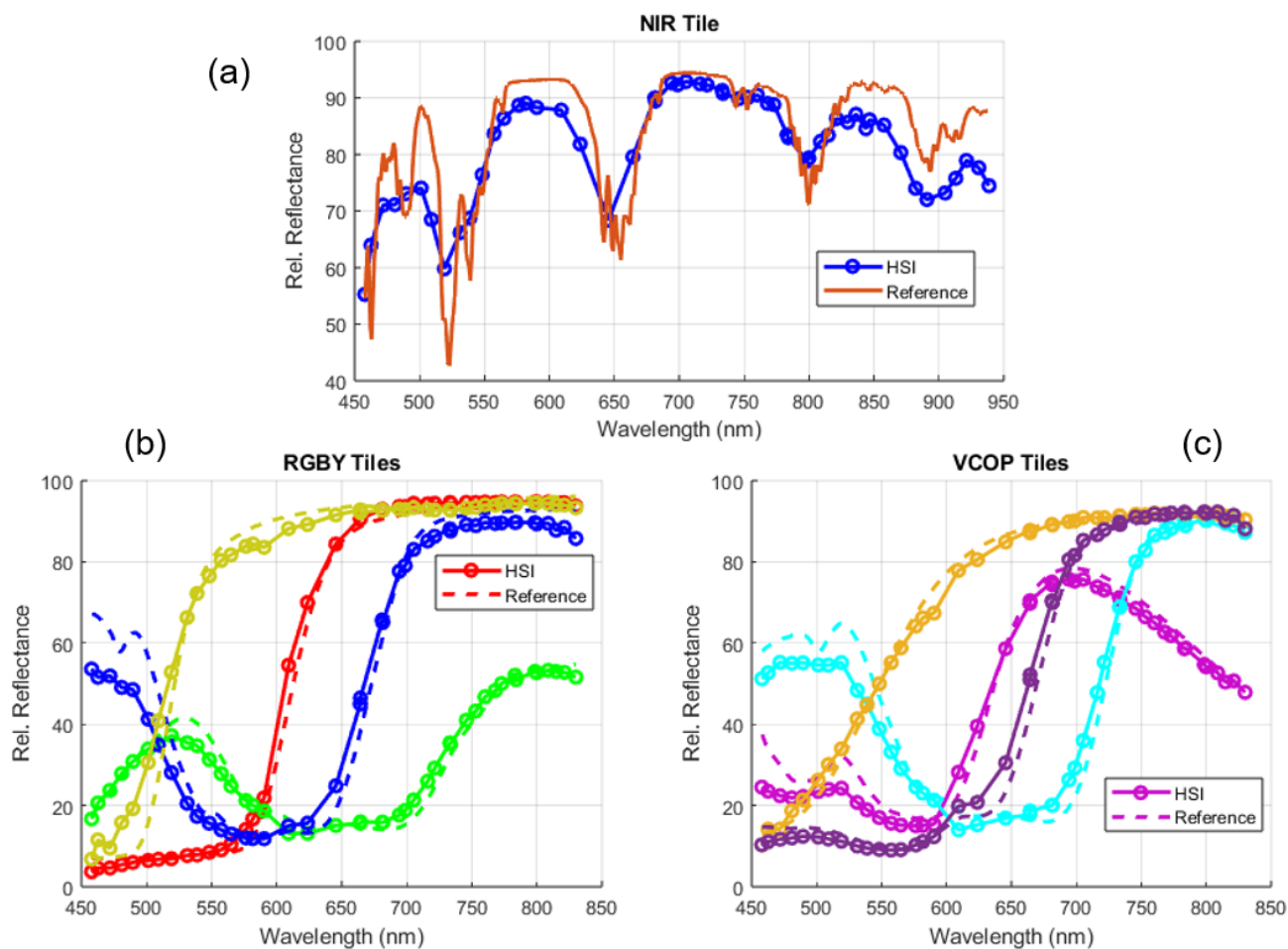


Figure 2. Results of spectral accuracy of the hyperspectral imaging system against the tile standard reflectance values. A) NIR reflectance tile. B) Red, green, blue, yellow reflectance tiles. C) Violet, cyan, orange, purple reflectance tiles.

Table 2. RMSE for each reference tile.

Tile	RMSE
Red	3.797
Green	2.630
Blue	5.123
Yellow	5.179
Violet	3.780
Cyan	4.205
Orange	2.420
Purple	3.555
NIR	6.983

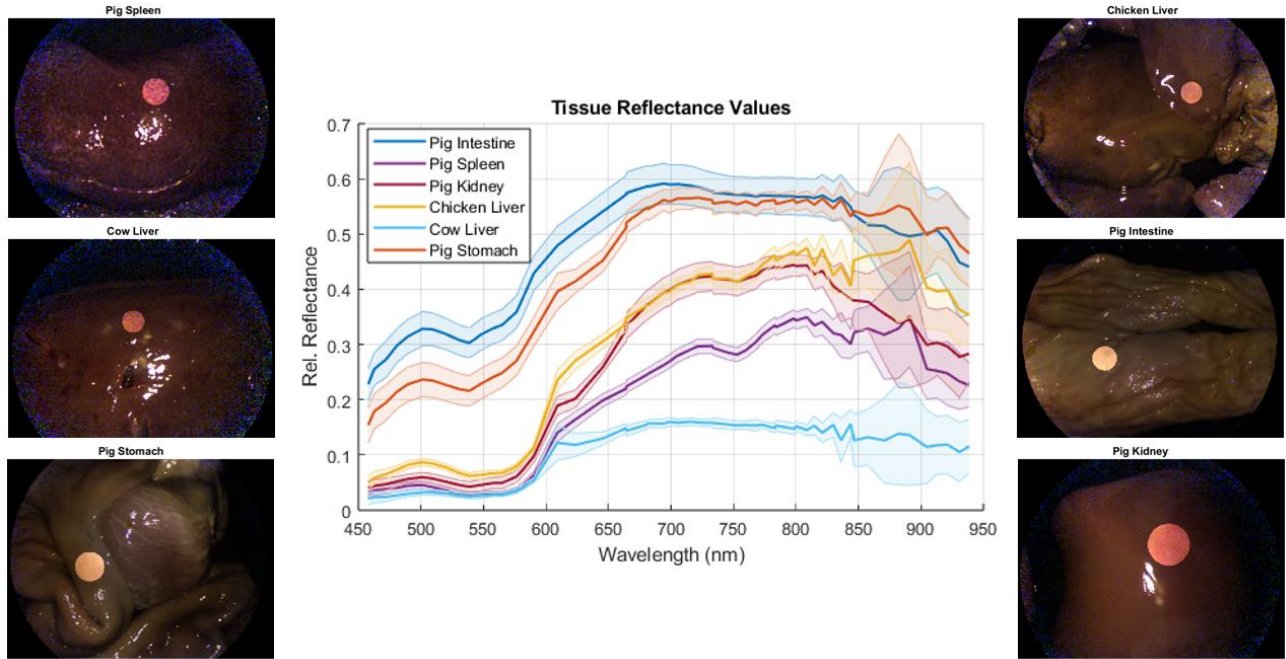


Figure 3. Pseudo-RGB images and the spectral curves of various tissues (Pig spleen, Cow liver, Pig stomach – left, Chicken liver, Pig intestine, Pig kidney – right) and spectral footprints within highlighted region of interest (center).

Table 3. Current distribution of abdominal *ex vivo* HSI dataset.

	Animal Models				Total
	Pig	Mouse	Chicken	Cow	
Stomach	86	29	-	-	115
Liver	176	96	399	233	904
Spleen	115	33	-	-	148
Kidney	135	34	-	96	265
Intestine	139	105	-	-	244
Pancreas	-	22	-	-	22
Uterus	83	33	-	-	116
Prostate + Seminal Vesicles	-	16	-	-	16
Bladder	-	5	-	-	5
Total	734	373	399	329	1835

4. DISCUSSION AND CONCLUSION

A high-speed hyperspectral imaging system was constructed and validated along with a framework for large-scale data acquisition. Spectral validation was shown for the captured wavelengths using standard reflectance tiles, showing sufficient sensitivity for the VIS, RNIR, and NIR snapshot imagers used in the system. Preliminary pseudo-RGB images of various tissues in the proposed dataset are shown along with regional spectral plotting, highlighting inherent distinctions in the backscattering characteristics of various tissues. The proposed system can be used to gather a robust hyperspectral

dataset of abdominal tissues for significant downstream applications such as identification of spectral signatures and deep learning-based tissue/organ classification.

In our survey of the current HSI datasets for deep learning applications, a clear gap between the fields of remote sensing and medical imaging was identified. Seeking to address this discrepancy and the lack of large-scale datasets in medical HSI, a novel hyperspectral imaging system for high-speed data acquisition using multiple snapshot hyperspectral imagers was developed and an *ex vivo* tissue dataset consisting of various abdominal and reproductive organs across four animal models was created. The system has been used alongside our developed software for high-throughput imaging, resulting in over 1800 hyperspectral images. Tissues can be processed efficiently through simultaneous imaging and semi-automatic processing pipelines for pseudo-RGB generation, hypercube registration and concatenation. The system maintains excellent spectral accuracy across all used reference tiles considering the added optics and decreased relative transmission from previous work. A limitation of the current work is the varying accessibility of tissues in the proposed dataset. Future work will include expanding the current dataset as this may lead to significant strides being made in HSI's ability to be used with modern deep learning methods for automatic identification of tissue and organs for surgical applications.

ACKNOWLEDGMENTS

Research reported in this publication was supported in part by the National Cancer Institute of the National Institutes of Health under Award Number R01CA288379 and R01CA204254 and by the Cancer Prevention and Research Institute of Texas (CPRIT) under Award Number RP240289 and RP240542. The content is solely the responsibility of the authors and does not necessarily represent the official views of the National Institutes of Health.

REFERENCES

- [1] G. Lu and B. Fei, "Medical hyperspectral imaging: a review," *J Biomed Opt*, vol. 19, no. 1, p. 10901, Jan 2014, doi: 10.1117/1.JBO.19.1.010901.
- [2] M. Halicek *et al.*, "Hyperspectral Imaging of Head and Neck Squamous Cell Carcinoma for Cancer Margin Detection in Surgical Specimens from 102 Patients Using Deep Learning," *Cancers (Basel)*, vol. 11, no. 9, Sep 14 2019, doi: 10.3390/cancers11091367.
- [3] S. Ortega *et al.*, "Hyperspectral Imaging for the Detection of Glioblastoma Tumor Cells in H&E Slides Using Convolutional Neural Networks," *Sensors (Basel)*, vol. 20, no. 7, Mar 30 2020, doi: 10.3390/s20071911.
- [4] M. H. Tran, L. Ma, J. V. Litter, A. Y. Chen, and B. Fei, "Thyroid Carcinoma Detection on Whole Histologic Slides Using Hyperspectral Imaging and Deep Learning," in *SPIE Medical Imaging*, San Diego, CA, Feb-Mar 2022, vol. 12039: Proc SPIE Int Soc Opt Eng, 2023/02/18 ed., PMC9929647, doi: 10.1117/12.2612963. [Online]. Available: <https://www.ncbi.nlm.nih.gov/pubmed/36798939>
- [5] M. Caron *et al.*, "Emerging properties in self-supervised vision transformers," in *Proceedings of the IEEE/CVF international conference on computer vision*, 2021, pp. 9650-9660.
- [6] M. Oquab *et al.*, "Dinov2: Learning robust visual features without supervision," *arXiv preprint arXiv:2304.07193*, 2023.
- [7] K. He, X. Chen, S. Xie, Y. Li, P. Dollár, and R. Girshick, "Masked autoencoders are scalable vision learners," in *Proceedings of the IEEE/CVF conference on computer vision and pattern recognition*, 2022, pp. 16000-16009.
- [8] J. Deng, W. Dong, R. Socher, L.-J. Li, K. Li, and L. Fei-Fei, "Imagenet: A large-scale hierarchical image database," in *2009 IEEE conference on computer vision and pattern recognition*, 2009: Ieee, pp. 248-255.
- [9] T.-Y. Lin *et al.*, "Microsoft coco: Common objects in context," in *Computer Vision—ECCV 2014: 13th European Conference, Zurich, Switzerland, September 6-12, 2014, Proceedings, Part V 13*, 2014: Springer, pp. 740-755.
- [10] B. Zhou, H. Zhao, X. Puig, S. Fidler, A. Barriuso, and A. Torralba, "Scene parsing through ade20k dataset," in *Proceedings of the IEEE conference on computer vision and pattern recognition*, 2017, pp. 633-641.
- [11] R. J. Chen *et al.*, "Towards a general-purpose foundation model for computational pathology," *Nature Medicine*, vol. 30, no. 3, pp. 850-862, 2024/03/01 2024, doi: 10.1038/s41591-024-02857-3.
- [12] M. Y. Lu *et al.*, "A visual-language foundation model for computational pathology," *Nature Medicine*, vol. 30, no. 3, pp. 863-874, 2024/03/01 2024, doi: 10.1038/s41591-024-02856-4.

- [13] H. Xu *et al.*, "A whole-slide foundation model for digital pathology from real-world data," *Nature*, pp. 1-8, 2024.
- [14] M. F. Baumgardner, L. L. Biehl, and D. A. Landgrebe, "220 Band AVIRIS Hyperspectral Image Data Set: June 12, 1992 Indian Pine Test Site 3," ed, 2015.
- [15] P. P. Gamba. *Pavia Centre and University Dataset*.
- [16] Y. Xu *et al.*, "Advanced multi-sensor optical remote sensing for urban land use and land cover classification: Outcome of the 2018 IEEE GRSS data fusion contest," *IEEE Journal of Selected Topics in Applied Earth Observations and Remote Sensing*, vol. 12, no. 6, pp. 1709-1724, 2019.
- [17] J. Ham, Y. Chen, M. M. Crawford, and J. Ghosh, "Investigation of the random forest framework for classification of hyperspectral data," *IEEE Transactions on Geoscience and Remote Sensing*, vol. 43, no. 3, pp. 492-501, 2005.
- [18] M. H. P. Fuchs and B. Demir, "HySpecNet-11k: a Large-Scale Hyperspectral Dataset for Benchmarking Learning-Based Hyperspectral Image Compression Methods," presented at the IGARSS 2023 - 2023 IEEE International Geoscience and Remote Sensing Symposium, 2023.
- [19] N. A. A. Braham, C. M. Albrecht, J. Mairal, J. Chanussot, Y. Wang, and X. X. Zhu, "SpectralEarth: Training Hyperspectral Foundation Models at Scale," *arXiv preprint arXiv:2408.08447*, 2024.
- [20] G. Sumbul, M. Charfuelan, B. Demir, and V. Markl, "Bigearthnet: A large-scale benchmark archive for remote sensing image understanding," in *IGARSS 2019-2019 IEEE International Geoscience and Remote Sensing Symposium*, 2019: IEEE, pp. 5901-5904.
- [21] H. Fabelo *et al.*, "In-vivo hyperspectral human brain image database for brain cancer detection," *IEEE Access*, vol. 7, pp. 39098-39116, 2019.
- [22] D. Wang *et al.*, "HyperSIGMA: Hyperspectral Intelligence Comprehension Foundation Model," *arXiv preprint arXiv:2406.11519*, 2024.
- [23] A. Studier-Fischer *et al.*, "HeiPorSPECTRAL-the Heidelberg porcine HyperSPECTRAL imaging dataset of 20 physiological organs," *Scientific Data*, vol. 10, no. 1, p. 414, 2023.
- [24] K. Pruitt *et al.*, "Design and validation of a high-speed hyperspectral laparoscopic imaging system," *Journal of Biomedical Optics*, vol. 29, no. 9, p. 093506, 2024. [Online]. Available: <https://doi.org/10.1117/1.JBO.29.9.093506>.
- [25] K. Pruitt *et al.*, "A dual-camera hyperspectral laparoscopic imaging system," presented at the Advanced Biomedical and Clinical Diagnostic and Surgical Guidance Systems XXII, 2024.
- [26] D. Mattes, D. R. Haynor, H. Vesselle, T. K. Lewellyn, and W. Eubank, "Nonrigid multimodality image registration," in *Medical imaging 2001: image processing*, 2001, vol. 4322: Spie, pp. 1609-1620.
- [27] M. Styner, C. Brechbuhler, G. Szckely, and G. Gerig, "Parametric estimate of intensity inhomogeneities applied to MRI," *IEEE transactions on medical imaging*, vol. 19, no. 3, pp. 153-165, 2000.